PNAS RESEARCH ARTICLE | APPLIED PHYSICAL SCIENCES

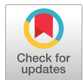

Gate-tunable contact-induced Fermi-level shift in semimetal

Xuanzhang Li[a], Yang Wei[a,1], Gaotian Lu[a], Zhen Mei[a], Guangqi Zhang[a], Liang Liang[a], Qunqing Li[a], Shoushan Fan[a], and Yuegang Zhang[a,b,1]

Edited by Hongjie Dai, Stanford University, Stanford, CA; received October 17, 2021; accepted March 16, 2022

Low-dimensional semimetal–semiconductor (Sm-S) van der Waals (vdW) heterostructures have shown their potentials in nanoelectronics and nano-optoelectronics recently. It is an important scientific issue to study the interfacial charge transfer as well as the corresponding Fermi-level shift in Sm-S systems. Here we investigated the gate-tunable contact-induced Fermi-level shift (CIFS) behavior in a semimetal single-walled carbon nanotube (SWCNT) that formed a heterojunction with a transition-metal dichalcogenide (TMD) flake. A resistivity comparison methodology and a Fermi-level catch-up model have been developed to measure and analyze the CIFS, whose value is determined by the resistivity difference between the naked SWCNT segment and the segment in contact with the TMD. Moreover, the relative Fermi-level positions of SWCNT and two-dimensional (2D) semiconductors can be efficiently reflected by the gate-tunable resistivity difference. The work function change of the semimetal, as a result of CIFS, will naturally introduce a modified form of the Schottky–Mott rule, so that a modified Schottky barrier height can be obtained for the Sm-S junction. The methodology and physical model should be useful for low-dimensional reconfigurable nanodevices based on Sm-S building blocks.

SWCNTs | 2D materials | Sm-S junctions | gate modulation

Significance

Resistivity comparison methodology was developed to measure and analyze the contact-induced Fermi-level shift (CIFS) as well as the interfacial charge transfer in low-dimensional semimetal–semiconductor (Sm-S) systems. The Fermi-level catch-up model was further built to depict the gate-tunable CIFS in such Sm-S systems. The Schottky barrier height for the Sm-S junction can be modified by introducing the CIFS term. The progress in this work will have an important role in promoting the research of Sm-S junctions, which are essential building blocks for future low-dimensional nanodevices.

Metal–semiconductor (M-S) junctions, one of the basic components of semiconductor devices, have been widely applied in electronic and optoelectronic devices, in which the Schottky barrier and interface quality could significantly contribute to the device function and performance (1). With the rise of two-dimensional (2D) materials and 2D electronics, various van der Waals (vdW) semimetals such as graphene (2–4), metallic carbon nanotubes (5, 6), and metallic transition-metal dichalcogenides (TMDs) (7–10), etc., have been used as electrodes for 2D semiconductors to build functional low-dimensional nanodevices. Benefiting from the specific semimetal–semiconductor (Sm-S) junctions, such nanodevices exhibit excellent performance due to the high-quality interfaces integrated via vdW interactions (11), the elimination of the Fermi-level pinning effect (12, 13), and the weak electrostatic screening effect (14, 15) of semimetal electrodes. In addition to the vertical field-effect transistors (FETs) (16–18), vertical tunneling FETs (15, 19), and photodetectors (20, 21) composed of vertically stacked graphene and 2D semiconductors, some important achievements have been made recently by employing the low-dimensional Sm-S heterostructures to optimize device performance and develop additional types of devices. Shen et al. (13) reported ultralow contact resistance between monolayer semiconductors and semimetal bismuth contacts, which could be attributed to the fact that the finite density of states (DOS) of the semimetal suppresses the metal-induced gap states and thus efficiently eliminates the Fermi-level pinning effect. Qiu et al. (22) developed graphene as a Dirac source for a semiconducting carbon nanotube (CNT) acquiring subthreshold swing (SS) of 40 mV/dec for CNT switches. Furthermore, mixed-dimensional heterostructures made of metallic CNT and semiconducting TMDs have exhibited reconfigurable functions as photodetectors (23, 24). All the progress indicates that Sm-S junctions will have important application prospects in future nanoelectronics and nano-optoelectronics.

The quantum capacitance effect (14) of semimetals with finite DOS makes the Sm-S systems different from the conventional M-S systems (25, 26) (Fig. 1). When a low-dimensional semimetal is in contact with a semiconductor, the misaligned Fermi levels will lead to spontaneous charge transfer at the Sm-S interface and result in a significant Fermi-level shift in semimetal naturally (Fig. 1 *B* and *C*). This behavior can be named contact-induced Fermi-level shift (CIFS) and is described by Eqs. **5–9** in *Materials and Methods*. In addition, the quantum capacitance effect also introduces an efficient modulation on Fermi levels of low-dimensional materials by an external electric field, which leads to a gate-tunable CIFS behavior in semimetals as well. Consequently, the shifted Fermi levels in semimetals induced by the gate potential and CIFS make the gate-tunable behaviors of the Sm-S junctions special in both the built-in electric field and the Schottky barrier height. The transport properties and optoelectrical properties of the Sm-S junctions might

Author affiliations: [a]State Key Laboratory of Low-Dimensional Quantum Physics, Department of Physics and Tsinghua-Foxconn Nanotechnology Research Center, Tsinghua University, Beijing 100084, China; and [b]Beijing Innovation Center for Future Chips, Tsinghua University, Beijing 100084, China

Author contributions: X.L., Y.W., and Y.Z. designed research; X.L., and Y.W. performed research; L.L., Q.L., and S.F. contributed new reagents/analytic tools; X.L., Y.W., G.L., Z.M., and G.Z. analyzed data; and X.L., Y.W., and Y.Z. wrote the paper.

The authors declare no competing interest.

This article is a PNAS Direct Submission.

Copyright © 2022 the Author(s). Published by PNAS. This article is distributed under Creative Commons Attribution-NonCommercial-NoDerivatives License 4.0 (CC BY-NC-ND).

[1]To whom correspondence may be addressed. Email: WeiYang@tsinghua.edu.cn or yuegang.zhang@tsinghua.edu.cn.

This article contains supporting information online at https://www.pnas.org/lookup/suppl/doi:10.1073/pnas.2119016119/-/DCSupplemental.

Published April 22, 2022.

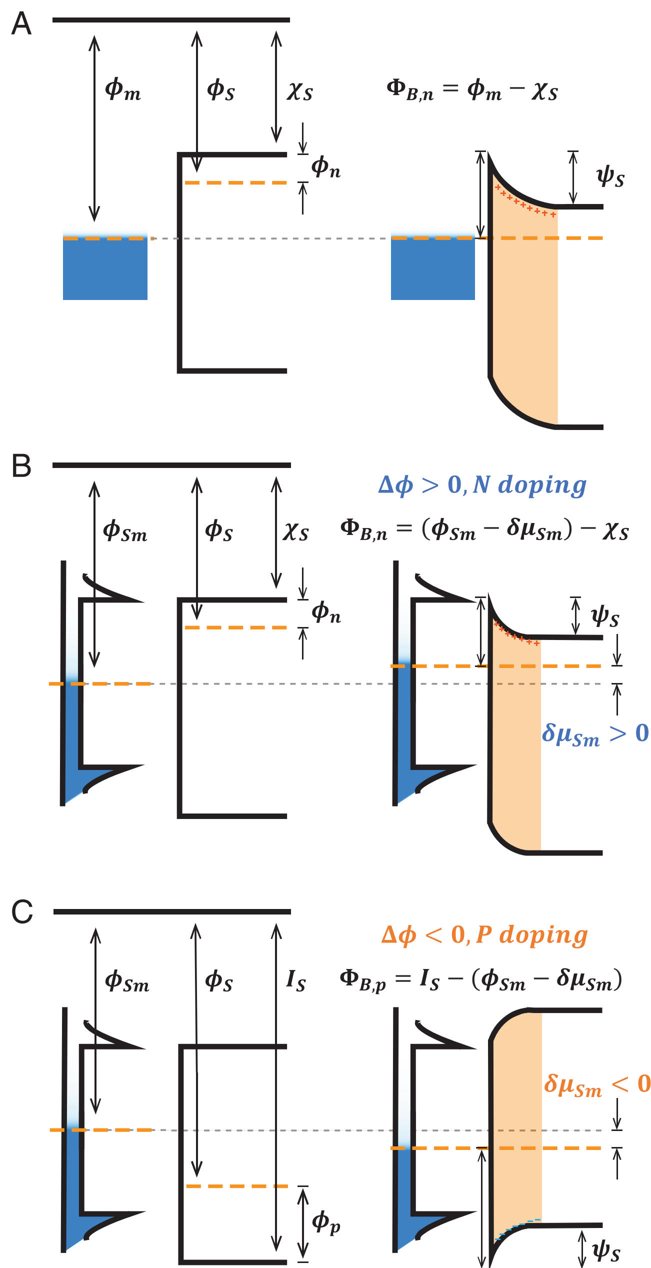

Fig. 1. (*A*–*C*) Characteristics of metal/semimetal–semiconductor junctions. Shown are band diagrams for classical metal–semiconductor junctions (*A*) and low-dimensional semimetal–semiconductor junctions (*B* and *C*) before and after junction formation. The contact-induced Fermi-level shift in semimetal as well as a smaller space charge region in semiconductor can be seen in the low-dimensional cases. *B* shows the case where the semimetal owns a larger work function while *C* represents the case where the semiconductor owns a larger work function.

also exhibit diverse behaviors. Hence, it is an important issue to develop an efficient methodology to study the CIFS behaviors as well as the interfacial charge transfer in Sm-S systems.

Here we employed a 1D-2D mixed-dimensional system to investigate CIFS in semimetals and interfacial charge transfer, in which a layered TMD flake (MoS_2 or WSe_2) was stacked on a semimetal single-walled carbon nanotube (SWCNT). A resistivity comparison methodology was developed to exhibit gate-tunable CIFS by comparatively studying electrical transport properties of the covered and naked SWCNT. A Fermi-level catch-up model based on band structures was further proposed to reveal the nature of the contact-induced resistivity difference, which agrees well with the experiment results and thus confirms the CIFS in SWCNT. By combining the resistivity comparison methodology and the Fermi-level catch-up model, the V_g -dependent relative Fermi-level positions of SWCNT and 2D semiconductors can be efficiently determined for both two-component and multicomponent systems, which is of great value for analyzing and revealing the operating mechanism of different van der Waals devices. In addition, the work function change of semimetal caused by CIFS will naturally introduce a modification term to the Schottky–Mott rule that revises the barrier height of the Sm-S junction. Our work deeply reveals the particularity of the Sm-S junctions and provides a reference for the construction of low-dimensional reconfigurable nanodevices.

Results

Resistivity Comparison Methodology. It is known that the transport behaviors of low-dimensional semimetals are sensitive to the gate potential (V_g), which can be attributed to their specific band structures and the quantum-capacitance–related Fermi-level shift. The transfer curves of metallic SWCNT and graphene show relative high resistivity when their Fermi levels are set around the Dirac point by V_g (27, 28). In addition to the gate modulation, interfacial charge transfer will also introduce a Fermi-level shift of such semimetals and a corresponding resistance change in the Sm-S systems. Fig. 1 schematically illustrates the band alignment of a semimetal SWCNT in contact with semiconductors, in which the CIFS $\delta\mu_{Sm}$ of the semimetal depends on the work function difference before contact ($\Delta\phi = \phi_{Sm} - \phi_S$). When the Fermi level of SWCNT is lower than that of the semiconductor, $\Delta\phi > 0$, electrons will transfer from semiconductor to semimetal, inducing N doping and a positive $\delta\mu_{Sm}$ for SWCNT, as shown in Fig. 1*B*. In the case of $\Delta\phi < 0$, $\delta\mu_{Sm} < 0$ and P doping is induced to SWCNT, as shown in Fig. 1*C*. In all these cases, the Fermi level of semimetal shifts away from its Dirac point, which brings a change of resistivity. Therefore, if the resistivity difference of semimetal with and without semiconductor contacting can be measured, behaviors of the interfacial charge transfer as well as the gate-tunable CIFS $\delta\mu_{Sm}$ of the semimetal could possibly be revealed efficiently. Therefore, the resistivity comparison methodology is suggested and developed to study these issues.

A 1D-2D mixed-dimensional system was constructed to investigate the CIFS and interfacial charge transfer in Sm-S heterostructures. Fig. 2*A* sketches the device structure and presents a scanning electron microscopy (SEM) image of such a device, where a stacked SWCNT-TMD heterostructure is wired by a series of well-designed electrodes. The fabrication procedures mainly include dry transfer techniques of CNT and TMD, and e-beam lithography (EBL). Briefly, an individual ultralong suspending metallic SWCNT was identified, picked up, and then transferred to the Si/SiO_2 substrate by two tungsten tips. A dry transfer method via polydimethylsiloxanes (PDMS) stamp was then used to stack a mechanically exfoliated MoS_2 flake onto the CNT. The Ti/Au (5/50 nm) electrodes were fabricated by using EBL, electron beam evaporation, and lift-off procedures. Raman spectroscopy (Fig. 2*B*) gives the identification for the metallic SWCNT (29, 30), MoS_2 and WSe_2 (31). The prominent radial breathing mode (RBM) peak verifies that the CNT is single walled, and the absence of the D peak around 1,350 cm^{-1} indicates the high quality of the CNT structure.

The as-fabricated device provides an effective solution for the comparative studies on CNT with and without MoS_2 contacting. The CNT is divided into segments by the Ti/Au electrodes. The five electrodes from B to F define four CNT segments with different lengths. All the transport measurements were conducted under vacuum at room temperature. The quasi-1D electronic

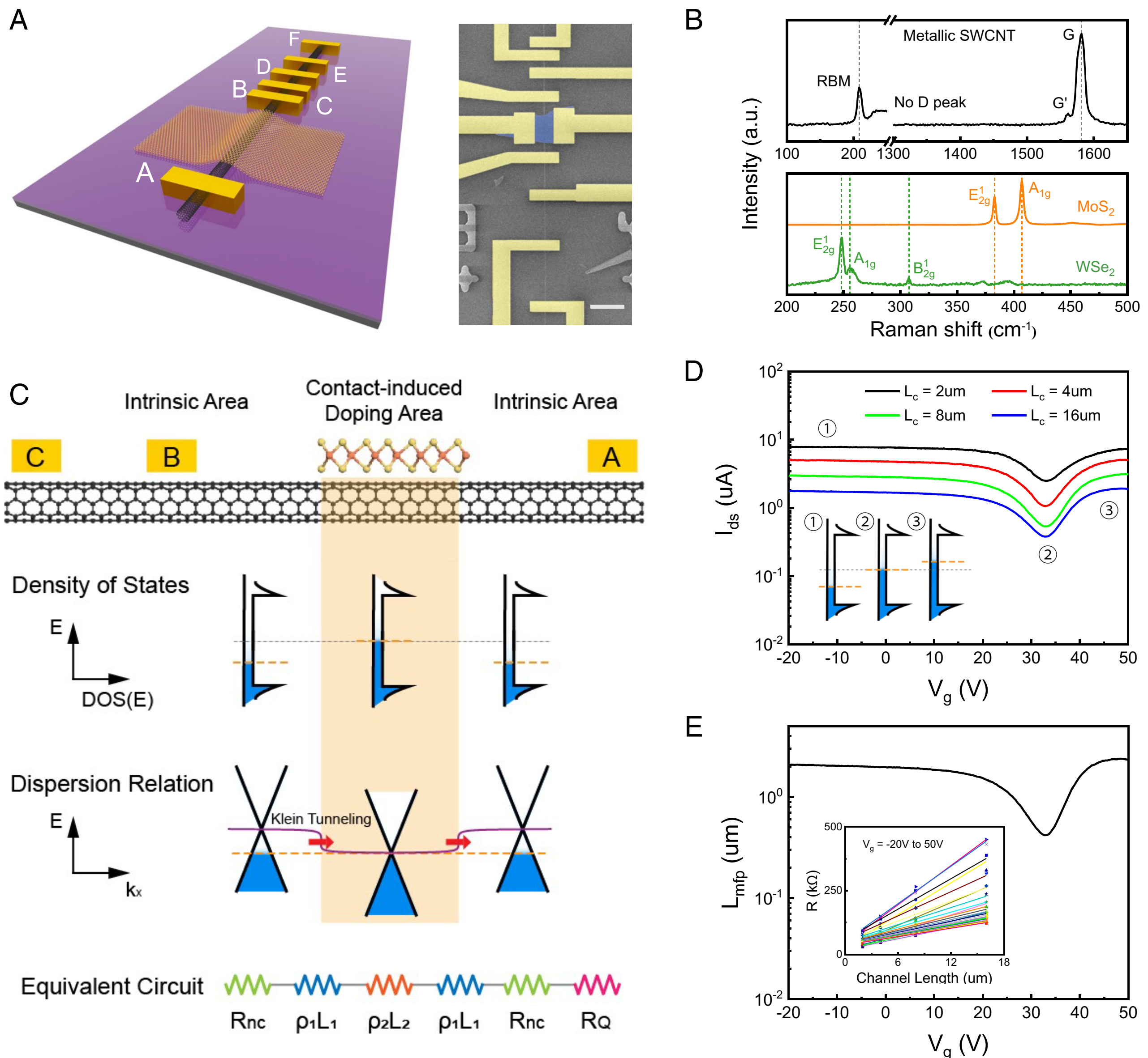

Fig. 2. Device structure and characterization. (*A*) Schematic and false color SEM image of SWCNT/MoS_2 device fabricated on the Si/300-nm SiO_2 substrate. (Scale bar: 10 μm.) (*B*) Raman spectra of individual metallic SWCNT and few-layer MoS_2, WSe_2 using a 532-nm laser. (*C*) Cross-sectional image and equivalent circuit of SWCNT/MoS_2 device, density of states, and dispersion relation of the metallic SWCNT. (*D*) Transfer characteristics of the SWCNT transistors with different channel lengths. (*E*) The extracted mean-free path of electrons in metallic SWCNT. *Inset* shows the transfer length method plot of total resistance versus channel length corresponding to each V_g from –20 to 50 V.

structures of metallic CNTs give small and constant DOS between the two first von Hove singularities, as sketched in Fig. 2*C* (32, 33). And there is an additional narrow gap about several tens of millielectonvolts ($\approx k_B T$) at the Dirac point due to curvature and strain (34). Such specific band structures make a small on/off ratio that could always be observed in transfer characteristics of metallic SWCNT devices, as shown in Fig. 2*D*. The length-dependent resistance derived from Fig. 2*D* was further plotted in Fig. 2 *E*, *Inset*, and the contact resistance (*SI Appendix*, Fig. S3), the channel resistivity (Fig. 3*A*) as well as the mean-free path of electrons (Fig. 2*E*) can be extracted from the intercepts and slopes according to the transfer length method (35). More information about the transfer length method can be found in *Materials and Methods*. The CNT segment covered by MoS_2 was wired by two electrodes A and B at the two naked parts. As shown in Fig. 2*C*, the resistance between electrodes A and B is equivalent to the sum of the contact resistance between SWCNT and Ti/Au, the resistance of intrinsic naked SWCNT, and the resistance of SWCNT in contact with MoS_2. Note that the resistance induced by the scattering at the junctions between covered CNT and naked CNT was neglected due to the linear dispersion relationship of the metallic SWCNT and the mismatched momentum between its two conducting channels (36–38). The Dirac electrons can pass through the barrier through Klein tunneling without backscattering (Fig. 2*C*) (39–41), which could be verified by the micrometer-long mean-free path of electrons (Fig. 2*E*) and the perfect linear output characteristics of the CNT segment defined by electrodes A and B (*SI Appendix*, Fig. S4 *C* and *D*). Therefore, the resistance as well as the resistivity (Fig. 3*B*) of the covered CNT can be calculated by subtracting the other items as shown in Fig. 2*C* from the resistance between A and B. The resistivity of the CNT with and without MoS_2 contacting is comparatively plotted in Fig. 3*C*.

Some critical information of the CIFS can be obtained from the V_g -dependent contact-induced resistivity difference of the

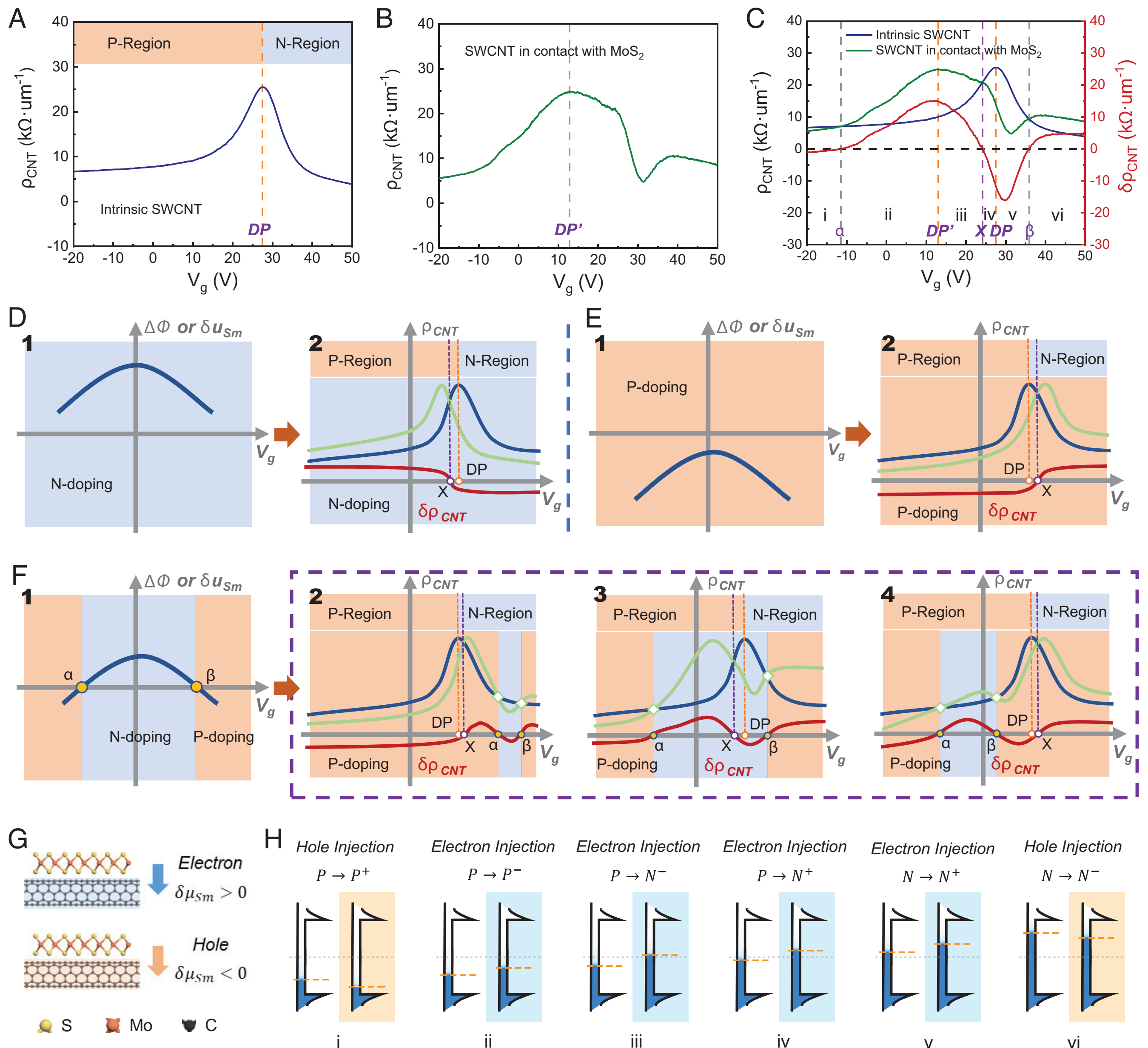

Fig. 3. Contact-induced Fermi-level shift behavior in semimetal SWCNT. (*A*) Experimentally measured resistivity of the intrinsic SWCNT. The top two color blocks represent conducting type (orange, hole; blue, electron). (*B*) Experimentally measured resistivity of the SWCNT that is in contact with MoS_2. (*C*) Resistivity comparison. Shown is measured resistivity of the SWCNT with (blue curve) and without (green curve) MoS_2 contacting as well as the contact-induced resistivity difference $\delta\rho$ (red curve). All the data were measured under V_{ds} = 100 mV. The reference lines are used to mark the location of the critical points (yellow, Dirac points; purple, X point; gray, α, β points). (*D–F*) Schematic of theoretical ergodic situations of the Fermi-level catch-up model. *D1*, *E1*, and *F1* present the three situations for work function difference $\Delta\phi$ or CIFS $\delta\mu_{Sm}$, respectively. The theoretical deduced contact-induced resistivity differences are plotted in *D2*, *E2*, *F2*, *F3*, and *F4*, where the blue, green, and red curves correspond to those in *C*. (*G*) Schematic of charge transfer and CIFS $\delta\mu_{Sm}$ of the Sm-S junction. (*H*) Schematic of the contact-induced Fermi-level shift behavior in semimetal SWCNT under different V_g.

semimetal in such a 1D-2D Sm-S system (Fig. 3 *A*–*C*). First, the shape of the two resistivity plots shows obvious differences. The ρ_{CNT} (V_g) plot of the intrinsic SWCNT (blue curve in Fig. 3 *A* and *C*) without semiconductor contacting shows a maximum value at the Dirac point, while there is a maximum value and an additional minimal value in the comparative plot for the SWCNT in contact with MoS_2 (green curve in Fig. 3 *B* and *C*). The significant change of the resistivity characteristics indicates a complicated behavior about the V_g -dependent CIFS in the semimetal SWCNT. Second, the two comparative plots have the same maximum resistivity at the Dirac points. Since the CIFS changes the Fermi-level position of the semimetal SWCNT rather than the band structure, the maximum value of the resistivity of the two SWCNT parts should be the same and appear at the position of their Dirac points. This could be used to verify the correctness of our resistivity measurement method. Third, the contact-induced resistivity difference $\delta\rho$ is also plotted in Fig. 3*C* (red curve). The value of $\delta\rho$ can be either positive or negative depending on the gate potential, which indicates that the CIFS depends on the gate potential and the two original Fermi levels in the Sm-S system may experience a complicated catch-up procedure under the gate modulation, which is discussed next.

Fermi-Level Catch-Up Model. From the respective band structures of the semimetal and semiconductor components, the gate-dependent CIFS $\delta\mu_{Sm}$ can be theoretically predictable for a

Sm-S junction. Before junction formation, the Fermi-level positions (μ) and the work functions ($\phi = 0 - \mu$) of the two materials can be independently controlled by V_g through the electrostatic capacitance effect following $d\mu/(e \cdot dV_g) = -d\phi/(e \cdot dV_g)$ = $C_g/(C_Q + C_g)$, where C_g and C_Q are the gate capacitance and the quantum capacitance, respectively (42). Since the metallic SWCNT has a constant DOS (constant C_Q) and the carriers in an N-type MoS_2 follow the Boltzmann distribution at room temperature (1), the derivatives of ϕ are

$$\frac{d\phi_{CNT}}{dV_g} = -A \quad [1]$$

$$\frac{d\phi_{MoS_2}}{dV_g} = -\frac{kT}{V_g + B}. \quad [2]$$

The work function difference between the CNT and MoS_2, defined as $\Delta\phi = \phi_{CNT} - \phi_{MoS_2}$, can thus be derived as

$$\Delta\phi = C + kTln(V_g + B) - AV_g, \quad [3]$$

where A, B, and C are all constants determined by materials and device structures. The curve drawn by Eq. **3** opens down like a downward parabola. Fig. 3 *D1*, *E1*, and *F1* shows three representative cases for $\Delta\phi$ and the doping states of the CNT after contact with MoS_2. Note that the orange and blue shaded areas represent the contact-induced P-type and N-type doping, respectively. Fig. 3 *D1* shows the case of $\Delta\phi > 0$ for all V_g, which indicates that the Fermi level of the CNT is lower than that of MoS_2 and electrons are injected into the CNT from MoS_2 after contacting. The contact thus introduces an equivalent N-type doping to the CNT and induces a Fermi-level lifting ($\delta\mu_{Sm} > 0$). Fig. 3 *E1* presents the case of $\Delta\phi < 0$ for all V_g. The CNT feels equivalent P-type doping and $\delta\mu_{Sm} < 0$, and the whole panel is marked in orange. Fig. 3 *F1* shows that the equation $\Delta\phi = 0$ has two solutions α and β. In the orange area ($V_g < \alpha$ and $V_g > \beta$), $\Delta\phi < 0$ and $\delta\mu_{Sm} < 0$, holes are injected into the CNT inducing equivalent P-type doping. In the blue area ($\alpha < V_g < \beta$), $\Delta\phi > 0$ and $\delta\mu_{Sm} > 0$, it turns to N doping. At α and β, $\Delta\phi = 0$, $\delta\mu_{Sm} = 0$, and there is no charge transfer. Therefore, the CIFS $\delta\mu_{Sm}$ has a similar dependency on V_g to that of $\Delta\phi$ in the above three cases, which can be further verified by Eq. **9** in *Materials and Methods*.

The contact-induced resistivity difference $\delta\rho$ can also be deduced from the as-established V_g -dependent CIFS $\delta\mu_{Sm}$. The $\rho - V_g$ curve of intrinsic CNT shown in Fig. 3*A* was used as a reference for theoretical deduction, with the orange and blue color blocks representing hole and electron conducting, respectively. Fig. 3 *D2*, *E2*, and *F2–F4* lists five representative cases of V_g -dependent ρ with (green curves) and without (blue curves) contacting as well as the corresponding $\delta\rho$ (red curves). In these panels, the top two color blocks indicate the intrinsic CNT conducting type and the bottom color blocks present the contact-induced doping type. Fig. 3 *D2* and *E2* corresponds to the cases of $\delta\mu_{Sm} > 0$ and $\delta\mu_{Sm} < 0$, respectively. There are three more cases for the $\pm$ switching of $\delta\mu_{Sm}$, including the Dirac point located in the N-doping region (Fig. 3 *F3*), the left P-doping region (Fig. 3 *F2*), and the right P-doping region (Fig. 3 *F4*). These qualitative deductions about $\rho - V_g$ are based on three basic principles. First, the position of the Dirac point shifts to the left when the CNT is N doped and to the right when it is P doped. Then the two transfer curves intersect at the point X, where the naked and MoS_2 -covered CNTs have different conducting types but the same resistivity, revealing that their Fermi levels are symmetric with respect to the Dirac point. Second, when the conducting type and the contact-induced doping type of the CNT are the same, the resistivity decreases; otherwise, the resistivity increases. This can be clearly seen by comparing the top and bottom block colors. The same color corresponds to a negative $\delta\rho_{CNT}$, and the different color corresponds to a positive $\delta\rho_{CNT}$. Third, the green and blue ρ_{CNT} curves intersect at points α and β, where $\delta\mu_{Sm} = 0$ and there is no contact-induced doping to the CNT. For a better understanding, Movies S1–S5 demonstrate the five cases.

The correctness of the theoretical analysis can be verified with experiment results. It can be found that almost all features of Fig. 3 *F3* are in accord with the experimental results shown in Fig. 3*C*, including the shape of the curves and the five feature points X, α, β, DP, and DP′. The theoretical analysis about CIFS $\delta\mu_{Sm}$ and contact-induced resistivity difference $\delta\rho$ in the CNT is built on the V_g -dependent Fermi-level misalignment $\Delta\phi$ between the CNT and MoS_2. Their band structures' difference shows different modulation efficiencies on Fermi-level shifting (Eqs. **1** and **2**) and their Fermi levels thus experience a catch-up process during gate modulation. Hence, such a theory is vividly named the Fermi-level catch-up model. Fig. 3*C* is further divided into six regions by the five feature points for more specific discussion. The corresponding band diagrams of the naked and MoS_2 -covered CNTs are sketched in Fig. 3*H*. Fig. 3 *H*, *i* indicates that the Fermi level of the CNT is higher than that of MoS_2 ($\Delta\phi < 0$), the P-type CNT receives a hole injection, the P doping is enhanced, and the conductivity is improved. In Fig. 3 *H*, *i* and *ii*, MoS_2 's Fermi level catches up with and surpasses the CNT at α. Fig. 3 *H*, *ii* represents that the P-type SWCNT accepts electron injection, the P doping is weakened, and the conductivity is reduced. Then the conductive type switching occurs in Fig. 3 *H*, *iii* and *iv*. Fig. 3 *H*, *iii* corresponds to the P-type SWCNT receiving electron injection, which reverses into a weaker N type with reduced conductivity. And a stronger N type with increased conductivity is achieved in Fig. 3 *H*, *iv*. Entering Fig. 3 *H*, *v*, the N-type SWCNT accepts electron injection, making the N type enhanced and conductivity improved. From Fig. 3 *H*, *v* to *vi*, the CNT's Fermi level overtakes MoS_2 at β. The N-type SWCNT receives hole injection again in Fig. 3 *H*, *vi* with weakened N doping and reduced conductivity. Therefore, when V_g is scanned from –20 to 50 V, the Fermi levels of the CNT and MoS_2 experience a process of overtaking and being overtaken, which leads to twice switching of the CIFS direction and can also be visually discriminated by the background colors of the band diagrams. Fig. 3*C* shows that the Dirac point of the CNT is located in the N-doping region (Fig. 3 *F3*) and the other cases could possibly be realized by changing the doping level of the CNT and MoS_2. For instance, the case presented in Fig. 3 *F4* has been experimentally implemented by introducing extra N doping to the SWCNT/MoS_2 junction; the Fermi level of the CNT reaches its Dirac point at negative V_g, and all the features of the ρ (V_g) curves shown in *SI Appendix*, Fig. S6 agree well with the prediction. More scenarios could be theoretically accessible via employing appropriate semimetals and semiconductors.

The Fermi-level catch-up process around point α was further verified by Kelvin probe force microscopy (KPFM). The surface potential images of the MoS_2 around the Sm-S junction and the corresponding line profiles are presented in Fig. 4, in which V_g varies from –30 to 20 V in steps of 10 V. It can be found that the surface potential difference between the Sm-S junction and the MoS_2 background can be efficiently modulated by V_g. The potential drops about 10 mV at V_g = –30 V on the lower-V_g side of α. This originates from the negatively charged MoS_2 surface induced by the electron transfer from SWCNT to MoS_2, since the Fermi level of the SWCNT is higher than

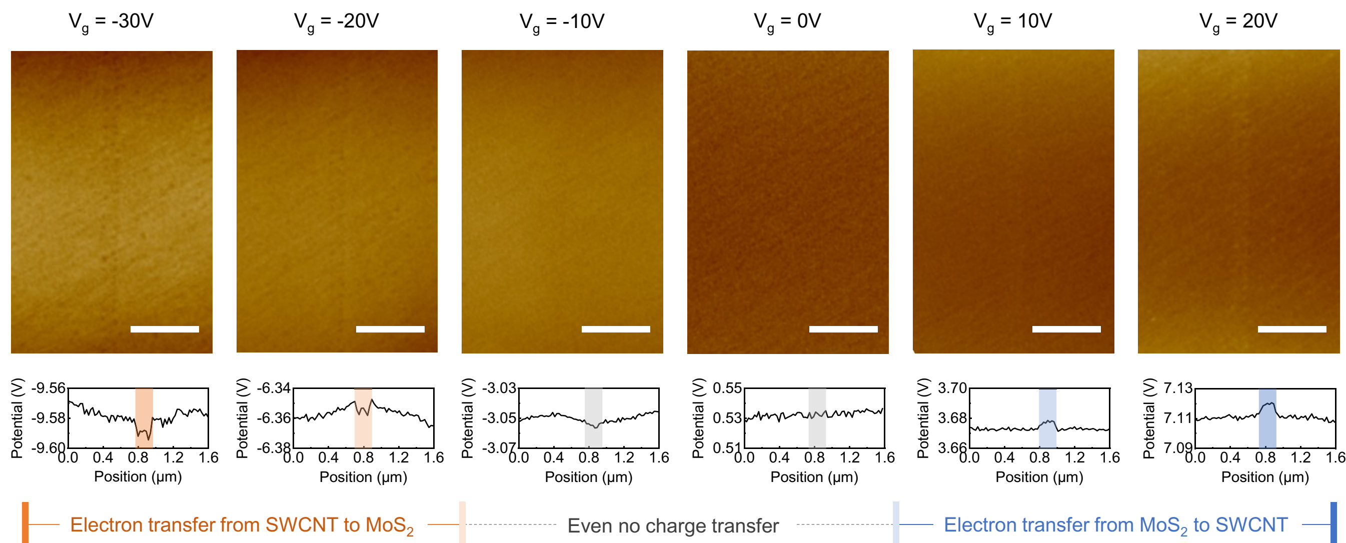

Fig. 4. Surface potential measurements by KPFM. Shown are potential mapping images of the MoS_2 around the Sm-S junction and the corresponding line profiles under different gate potentials. Different electron transfer directions are marked by the orange (from SWCNT to MoS_2) and blue (from MoS_2 to SWCNT) backgrounds, respectively. (Scale bar: 1 μm.)

that of MoS_2 at this region. Their Fermi levels meet at α around −10 to 0 V, where the potential difference disappears (the third and fourth panels in Fig. 4). A reversed contrast of the Sm-S junction appears in the potential images at V_g = 10 and 20 V, which can be attributed to the Fermi level of MoS_2 overtaking the SWCNT, inducing a positively charged MoS_2 surface around the CNT. These results qualitatively agree well with the ρ (V_g) curves shown in Fig. 3*C*. More detailed information about the measuring system and sample can be found in *Materials and Methods* and *SI Appendix*.

Determination of the Relative Fermi-Level Positions. By combining the resistivity comparison methodology and the Fermi-level catch-up model, the V_g -dependent relative Fermi-level positions of the SWCNT and semiconductor can be efficiently obtained. For the two-component system, the intuitive rule can be summarized from Fig. 3 *C* and *H*. The X point should be set as a critical point. On its lower-V_g side, larger resistivity corresponds to higher Fermi-level position; while on the higher-V_g side, the reverse applies. This strategy can be further applied to the multicomponent system, where several 2D semiconductors are stacked on different segments of a single SWCNT. Since different 2D materials have the same CNT as a reference, their relative Fermi-level positions can thus be determined by the rules of the two-component system. As an embodiment, SWCNT/MoS_2 and SWCNT/WSe_2 heterojunctions were fabricated on the same metallic SWCNT as shown in Fig. 5*A*. The extracted resistivity of intrinsic CNT as well as CNT segments in contact with MoS_2 and WSe_2 are comparatively plotted in Fig. 5*B*. The $\delta\rho$ as function of V_g is plotted in Fig. 5*C* with the contact-induced P-type and N-type doping regions marked by orange and blue backgrounds, respectively. The resistivity difference $\delta\rho$ of the CNT in contact with MoS_2 is consistent with the device shown in Fig. 2*A*, while the one in contact with WSe_2 shows a significant difference. This difference should be attributed to the different band structures between WSe_2 and MoS_2. Detailed analysis can be found in *SI Appendix*. According to the $\rho - V_g$ plots and the above summarized rules, the V_g -dependent relative Fermi-level positions of intrinsic SWCNT, MoS_2, and WSe_2 can be resolved. Fig. 5*D* sketches the band diagrams before junction formation at six different V_g indicated by dashed lines in Fig. 5*B*. From $-V_g$ to $+V_g$, the relative Fermi-level positions experience $\phi_{MoS_2} > \phi_{CNT} > \phi_{WSe_2}$ at V_g = −30 V, $\phi_{CNT} = \phi_{MoS_2} > \phi_{WSe_2}$ at V_g = −21 V, $\phi_{CNT} > \phi_{MoS_2} = \phi_{WSe_2}$ at V_g = −13.5 V, $\phi_{CNT} > \phi_{WSe_2} > \phi_{MoS_2}$ at V_g = 0 V, $\phi_{CNT} = \phi_{MoS_2} = \phi_{WSe_2}$ at V_g = 22.3 V, and $\phi_{MoS_2} > \phi_{WSe_2} > \phi_{CNT}$ at V_g = 30 V, respectively. This information will be of great importance to reveal the operating mechanism of multifunctional or reconfigurable devices based on vdW heterojunctions.

The band structures and Fermi-level positions of TMDs depend on their layer number, which can also be discriminated effectively by the strategy. MoS_2 flakes with different thickness (3L and 8 nm) were stacked on a same metallic SWCNT as shown in *SI Appendix*, Fig. S9*A*. The CIFS in the SWCNT induced by the two MoS_2 flakes was further studied and the comparative resistivities are plotted in *SI Appendix*, Fig. S9*C*. The relative Fermi-level positions and the Fermi level catch-up process of the three materials can thus be deduced, which is sketched in *SI Appendix*, Fig. S9*D*. Compared with 8 nm MoS_2, the Fermi level of 3L MoS_2 is lower at V_g = −30 V, but higher at V_g = 30 V. This reveals that the 3L MoS_2 owns a higher conduction band edge and a lower valence band edge, which is consistent with previous reports (43). All the results show that the as-developed strategy has great abilities in resolving the Fermi-level positions as well as providing rich information on the Fermi-level catch-up process in the low-dimensional systems.

Discussion

The CIFS in semimetal is prevalent in Sm-S systems for their finite DOS. Similar CIFS behaviors as metallic SWCNT have also been observed in MoS_2 -covered graphene by using the resistivity comparison methodology. The detailed information about the graphene/MoS_2 specimen and the ρ (V_g) curves with four feature points (X, β, DP, and DP′) are shown in *SI Appendix*, Fig. S10. Considering the C_Q of graphene (7 $\mu F/cm^2$) (44), the modulation of its Fermi level should be within ±50 mV in our experiment. In this range, the variation of C_Q is not significant and Eqs. **1** and **2** also apply; thus the comparative resistivity plots in *SI Appendix*, Fig. S10*D* approximate the theoretical deduction (Fig. 3 *F3*). However, the feature point α is absent in this V_g range, which can be attributed to the different band structure between

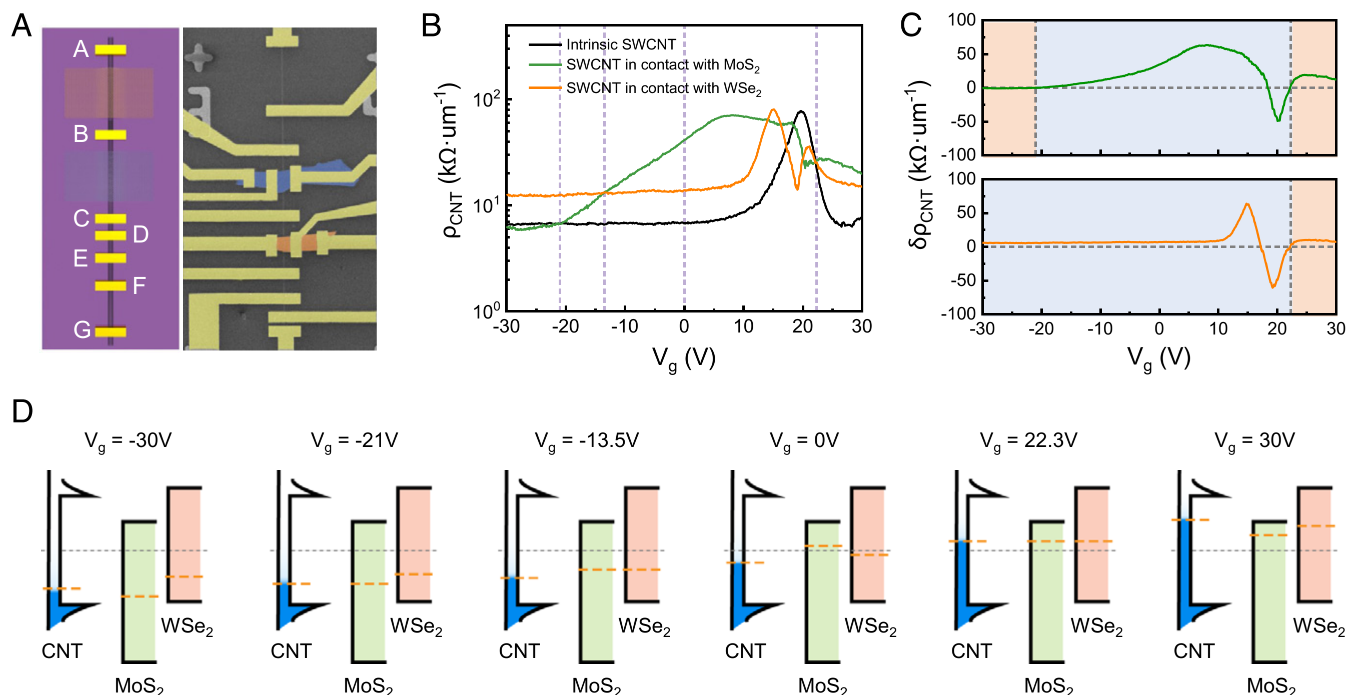

Fig. 5. Individual semimetal SWCNT in contact with MoS_2 and WSe_2. (*A*) Schematic illustration and false color SEM image of the heterojunction device. The MoS_2 flake is emphasized by the blue blocks and the WSe_2 by the orange blocks. (*B*) Experimentally measured resistivity of the SWCNT in the three different segments. All the data were measured under V_{ds} = 100 mV. (*C*) The resistivity difference $\delta\rho$ of the SWCNT by contacting with MoS_2 and WSe_2. (*D*) Schematic illustrations of the deduced Fermi-level positions of SWCNT, MoS_2, and WSe_2 under different V_g.

the graphene and SWCNT and the screening effect induced by underlying graphene.

Because of the CIFS behavior in semimetal, it is necessary to introduce a modification to the Schottky–Mott rule for the low-dimensional Sm-S junctions. The barrier height at the Sm-S interface should be expressed as $\Phi_B = (\phi_{Sm} - \delta\mu_{Sm}) - \chi_S$, where the CIFS $\delta\mu_{Sm}$ is a modification term for semimetal work function and actually reflects the direction of the built-in electric field in the semiconductor (*SI Appendix*, Fig. S11*C*). The barrier height depends on the gate potentials, since both the work functions of semimetal ϕ_{Sm} and $\delta\mu_{Sm}$ are gate tunable. The modified rule for Sm-S junctions is significantly different from that for the traditional M-S junctions and it could serve as a fundamental theoretical rule for analyzing low-dimensional nanodevices.

Conclusion

In summary, we fully discussed the Fermi-level shift behavior in low-dimensional Sm-S junctions represented by SWCNT/MoS_2, SWCNT/WSe_2, and graphene/MoS_2. An efficient resistivity comparison methodology to study the CIFS as well as the interfacial charge transfer has been developed. The Fermi-level catch-up model reveals that the complex resistivity difference of the SWCNT originates from the gate-tunable Fermi-level misalignment between the semimetal and the semiconductor. A simple but effective rule was further developed to efficiently determine the relative Fermi-level positions between CNT and 2D materials at specific gate voltages, which is applicable for both two- and multicomponent systems. In addition, the CIFS in semimetal introduces a modification to the Schottky–Mott rule, giving an accurate expression for the Schottky barrier height of the Sm-S junction. The progress in this paper has an important role in promoting the research on Sm-S junction, which will be the essential building blocks for future low-dimensional nanodevices.

Materials and Methods

Origin of CIFS $\delta\mu_{Sm}$ and Modification to the Schottky–Mott Rule. The low-dimensional semimetal with half-filled energy band has finite DOS near the pristine Fermi level, which means that the charge transfer could lead to a significant shift of Fermi level relative to the band. This phenomenon is called the quantum capacitance effect (14), which is defined as

$$C_Q = e\frac{dQ}{d\mu} = e^2\frac{dn}{d\mu}, \quad [4]$$

where Q, μ, and n are the net charge concentration, the chemical potential (Fermi level), and electron number density in low-dimensional materials. It can be simplified as $C_Q = e^2 DOS(\mu)$ at 0 K, and a more complex expression should be given as

$$C_Q(\mu, T) = e^2 \int d\mu' DOS(\mu')[-\frac{\partial f(\mu', T)}{\partial \mu'}] \quad [5]$$

at a certain temperature T due to the thermal broadening of Fermi distribution. That is, the quantum capacitance is positively correlated with DOS.

When a low-dimensional semimetal with finite DOS contacts a semiconductor, the misaligned Fermi level leads to spontaneous charge transfer at the interface to achieve thermodynamic equilibrium. Carrier depletion or accumulation occurs in the semiconductor at the interface; meanwhile, the transferred charge will naturally lead to the Fermi-level shift of the semimetal, making the Schottky barrier height (SBH) of the low-dimensional Sm-S junction deviate from the description of the classical Schottky–Mott rule, as shown in Fig. 1*B*. A modification term of semimetal work function $\delta\mu_{Sm}$ needs to be added.

The cases shown in Fig. 1 do not consider the influence of impurities, defects, and other interface states. The charge transfer process satisfies the charge conservation:

$$\Delta Q_{Sm} + \Delta Q_S = 0. \quad [6]$$

After contact, electrons transfer from semiconductor to (semi)metal, because of the higher work function of (semi)metal. Using the depletion layer approximation (1), the total charge transferred is

$$\Delta Q_S = eN_D W_D = \sqrt{e\varepsilon_S N_D \psi_S}, \quad [7]$$

where ψ_s is the band offset of the semiconductor at the space charge region, N_D is the donor concentration, W_D is the width of the space charge region, and ε_s represents the dielectric constant of the semiconductor. For (semi)metal, the differential relationship between charge filling and Fermi-level shift is $dQ = eDOS(\mu)d\mu = \frac{1}{e}C_Q(\mu)d\mu$. That is, the total transferred charge

$$\Delta Q_{Sm} = -\frac{1}{e}\int_{\mu_0}^{\mu_0+\delta\mu_{Sm}} C_Q(\mu, T)d\mu. \quad [8]$$

The CIFS is

$$\delta\mu_{Sm} = \Delta\phi - \psi_s. \quad [9]$$

In this case, the Schottky barrier height at the interface is

$$\Phi_B = (\phi_{Sm} - \delta\mu_{Sm}) - \chi_S. \quad [10]$$

If the parameters $\mu_0, T, \varepsilon_s, N_D, C_Q$, and ϕ_n were known, we can solve the band diagram completely combining Eqs. **5**–**10** and get definite values of $\delta\mu_{Sm}, \chi_S$, and Φ_B.

For metals, the quite large DOS around the Fermi level makes the C_Q tend to be infinity. According to Eq. **8**, we can get $\delta\mu_{Sm} \rightarrow 0$; that is, the Fermi level of traditional metal does not move, and the SBH of the metal–semiconductor junction is $\Phi_B = \phi_{Sm} - \chi_S$. When it comes to low-dimensional semimetals with finite C_Q, the modification term of work function $\delta\mu_{Sm}$ can be calculated through the equations above, the work function of the semimetal in the contact area is modified as $\phi'_{Sm} = \phi_{Sm} - \delta\mu_{Sm}$, and the SBH is $\Phi_B = \phi'_{Sm} - \chi_S$.

Extraction of Resistivity of SWCNT. The metallic SWCNT owns two conductive channels near the Fermi level, which determines a top conductivity value of $\frac{4e^2}{h}$; that is, a minimum quantum resistance $R_Q = 6.5k\Omega$. Resistance of a long-range SWCNT device can be expressed as (35)

$$R_{tot} = \frac{h}{4e^2}\frac{L}{L_{mfp}} + 2R_{nc} + R_Q, \quad [11]$$

where the first term on the right represents the wire resistance of the SWCNT channel, L is the channel length of the SWCNT, and L_{mfp} is the mean free path of electrons; the last two parts are the total contact resistance, and R_{nc} is the interfacial resistance caused by the imperfect contact between metal and SWCNT. According to Eq. **11**, we plot transfer characteristics of the four two-terminal devices with different channel lengths in Fig. 2*D* and then extract the contact resistance and channel resistivity corresponding to each electrostatic potential V_g through the transfer length method. Values of $\sim$0.3 to 16 $k\Omega$ and $\sim$0.5 to 2.5 μm for R_{nc} and L_{mfp}, respectively, have been extracted, which prove that the high-quality contact has been formed between the Ti and metallic SWCNT as well as the device owning micrometer-long ballistic transport capability.

Device Fabrication. The high-quality ultralong CNTs were grown in suspension using iron as catalyst and ethylene as carbon source. The metallic single-walled CNTs were selected by combining optical and electrical measurements and then transferred onto the target location on the Si/300-nm SiO_2 substrate using two tungsten tips. For the device shown in Fig. 2*A*, the dry transfer method via PDMS was used to stack the mechanically exfoliated MoS_2 flake onto the bottom CNT; while the wet method via PDMS/polyvinyl alcohol was used to pick up MoS_2 and WSe_2 flakes successively and then construct the heterojunctions shown in Fig. 5*A* with one step transfer. To achieve clean and tight van der Waals interface, the sample was annealed under vacuum (400 mTorr) at 350 °C for 1 h. Electrodes Ti/Au (5/50 nm) were fabricated through EBL, electron beam evaporation, and lift off. Another annealing process was performed to improve the contacts.

Characterization. Electrical measurements were carried out on a semiconductor analyzer (Agilent B1500A) combined with a Lakeshore CRX-4K under vacuum. SEM images were obtained on an FEI Nova NanoSEM 450 with accelerating voltage at 1 kV. Atomic force microscopy (AFM) images were carried out on a BRUKER icon in tapping mode. Raman spectroscopy was performed on a Horiba Jobin Yvon LabRAM HR 800 with a 532-nm focused laser.

KPFM measurements were performed under ambient conditions at room temperature and 10% relative humidity (RH). The potential images were obtained using Bruker Multimode 8 in tapping mode. The direct-current (DC) bias applied compensates the contact potential difference (CPD) between the tip and sample, $V_{DC} = -V_{CPD}$. The CPD can be expressed as $V_{CPD} = (\phi_{CNT} - \phi_{MoS_2})/q$, where q is elementary charge unit. The KPFM was conducted in amplitude modulation mode and the lift height was set to 100 nm. The probe is affected by the gate potential during the test, which limits the V_g range that can be applied to –30 to 20 V in our experiment.

Data Availability. All study data are included in this article and/or *SI Appendix*.

ACKNOWLEDGMENTS. We thank Y. Kong for her help and discussions in measuring Raman spectra and AFM images. We thank K. Liu and R. Peng for their help and discussions in KPFM measurements. This work was financially supported by the National Key Research and Development Program of China (Grant 2018YFA0208401), the National Natural Science Foundation of China (Grants 61774090, U1832218, and 51727805), the National Key Research and Development Program of China (Grants 2016YFB0100100 and 2017YFA0205803), and the Key-Area Research and Development Program of Guangdong Province (Grant 2020B010169001).

1. S. M. Sze, K. K. Ng, *Physics of Semiconductor Devices* (Wiley, Hoboken, NJ, 2006).
2. X. Cui *et al.*, Multi-terminal transport measurements of MoS_2 using a van der Waals heterostructure device platform. *Nat. Nanotechnol.* **10**, 534–540 (2015).
3. Y. Liu *et al.*, Toward barrier free contact to molybdenum disulfide using graphene electrodes. *Nano Lett.* **15**, 3030–3034 (2015).
4. L. Yu *et al.*, Graphene/MoS_2 hybrid technology for large-scale two-dimensional electronics. *Nano Lett.* **14**, 3055–3063 (2014).
5. J. Zhang *et al.*, SWCNT-MoS_2-SWCNT vertical point heterostructures. *Adv. Mater.* **29**, 1604469 (2017).
6. J. Zhang *et al.*, Carbon-nanotube-confined vertical heterostructures with asymmetric contacts. *Adv. Mater.* **29**, 1702942 (2017).
7. R. Kappera *et al.*, Phase-engineered low-resistance contacts for ultrathin MoS_2 transistors. *Nat. Mater.* **13**, 1128–1134 (2014).
8. R. Kappera *et al.*, Metallic 1t phase source/drain electrodes for field effect transistors from chemical vapor deposited MoS_2. *APL Mater.* **2**, 092516 (2014).
9. J. Li *et al.*, General synthesis of two-dimensional van der Waals heterostructure arrays. *Nature* **579**, 368–374 (2020).
10. S. Song *et al.*, Wafer-scale production of patterned transition metal ditelluride layers for two-dimensional metal–semiconductor contacts at the Schottky–Mott limit. *Nat. Electron.* **3**, 207–215 (2020).
11. A. K. Geim, I. V. Grigorieva, Van der Waals heterostructures. *Nature* **499**, 419–425 (2013).
12. S. W. LaGasse, P. Dhakras, K. Watanabe, T. Taniguchi, J. U. Lee, Gate-tunable graphene–WSe_2 heterojunctions at the Schottky–Mott limit. *Adv. Mater.* **31**, e1901392 (2019).
13. P. C. Shen *et al.*, Ultralow contact resistance between semimetal and monolayer semiconductors. *Nature* **593**, 211–217 (2021).
14. S. Luryi, Quantum capacitance devices. *Appl. Phys. Lett.* **52**, 501–503 (1988).
15. L. Britnell *et al.*, Field-effect tunneling transistor based on vertical graphene heterostructures. *Science* **335**, 947–950 (2012).
16. W. J. Yu *et al.*, Vertically stacked multi-heterostructures of layered materials for logic transistors and complementary inverters. *Nat. Mater.* **12**, 246–252 (2013).
17. T. Georgiou *et al.*, Vertical field-effect transistor based on graphene-WS2 heterostructures for flexible and transparent electronics. *Nat. Nanotechnol.* **8**, 100–103 (2013).
18. L. Liu *et al.*, Transferred van der Waals metal electrodes for sub-1-nm MoS_2 vertical transistors. *Nat. Electron.* **4**, 342–347 (2021).
19. L. Britnell *et al.*, Resonant tunnelling and negative differential conductance in graphene transistors. *Nat. Commun.* **4**, 1794 (2013).
20. L. Britnell *et al.*, Strong light-matter interactions in heterostructures of atomically thin films. *Science* **340**, 1311–1314 (2013).
21. W. J. Yu *et al.*, Highly efficient gate-tunable photocurrent generation in vertical heterostructures of layered materials. *Nat. Nanotechnol.* **8**, 952–958 (2013).
22. C. Qiu *et al.*, Dirac-source field-effect transistors as energy-efficient, high-performance electronic switches. *Science* **361**, 387–392 (2018).
23. K. Zhang *et al.*, Electrical control of spatial resolution in mixed-dimensional heterostructured photodetectors. *Proc. Natl. Acad. Sci. U.S.A.* **116**, 6586–6593 (2019).
24. J. Zhang *et al.*, Mixed-dimensional vertical point p-n junctions. *ACS Nano* **14**, 3181–3189 (2020).
25. W. Schottky, Zur halbleitertheorie der sperrschicht- und spitzengleichrichter. *Z. Phys. A* **113**, 367 (1939).
26. N. Mott, The theory of crystal rectifers. *Proc. R. Soc. Lond. A Math. Phys. Sci.* **171**, 27–38 (1939).
27. K. S. Novoselov *et al.*, Electric field effect in atomically thin carbon films. *Science* **306**, 666–669 (2004).
28. S. Ilani, P. L. McEuen, Electron transport in carbon nanotubes. *Annu. Rev. Condens. Matter Phys.* **1**, 1–25 (2010).
29. A. Jorio *et al.*, Structural (n, m) determination of isolated single-wall carbon nanotubes by resonant Raman scattering. *Phys. Rev. Lett.* **86**, 1118–1121 (2001).
30. M. Dresselhaus, G. Dresselhaus, R. Saito, A. Jorio, Raman spectroscopy of carbon nanotubes. *Phys. Rep.* **409**, 47–99 (2005).
31. P. Tonndorf *et al.*, Photoluminescence emission and Raman response of monolayer MoS_2, $MoSe_2$, and WSe_2. *Opt. Express* **21**, 4908–4916 (2013).
32. R. Saito, M. Fujita, G. Dresselhaus, M. S. Dresselhaus, Electronic structure of chiral graphene tubules. *Appl. Phys. Lett.* **60**, 2204–2206 (1992).

33. J. C. Charlier, X. Blase, S. Roche, Electronic and transport properties of nanotubes. *Rev. Mod. Phys.* **79**, 677–732 (2007).
34. M. Ouyang, J. L. Huang, C. L. Cheung, C. M. Lieber, Energy gaps in "metallic" single-walled carbon nanotubes. *Science* **292**, 702–705 (2001).
35. A. D. Franklin, Z. Chen, Length scaling of carbon nanotube transistors. *Nat. Nanotechnol.* **5**, 858–862 (2010).
36. T. Ando, T. Nakanishi, Impurity scattering in carbon nanotubes – Absence of back scattering –. *J. Phys. Soc. Jpn.* **67**, 1704–1713 (1998).
37. T. Ando, T. Nakanishi, Berry's phase and absence of back scattering in carbon nanotubes. *J. Phys. Soc. Jpn.* **67**, 2857–2862 (1998).
38. P. L. McEuen, M. Bockrath, D. H. Cobden, Y. G. Yoon, S. G. Louie, Disorder, pseudospins, and backscattering in carbon nanotubes. *Phys. Rev. Lett.* **83**, 5098–5101 (1999).
39. O. Klein, Die reflexion von elektronen an einem potentialsprung nach der relativistischen dynamik von dirac. *Z. Phys. A* **53**, 153–165 (1929).
40. M. I. Katsnelson, K. S. Novoselov, A. K. Geim, Chiral tunnelling and the Klein paradox in graphene. *Nat. Phys.* **2**, 620–625 (2006).
41. G. A. Steele, G. Gotz, L. P. Kouwenhoven, Tunable few-electron double quantum dots and Klein tunnelling in ultraclean carbon nanotubes. *Nat. Nanotechnol.* **4**, 363–367 (2009).
42. S. Ilani, L. A. K. Donev, M. Kindermann, P. L. McEuen, Measurement of the quantum capacitance of interacting electrons in carbon nanotubes. *Nat. Phys.* **2**, 687–691 (2006).
43. M. Chhowalla *et al.*, The chemistry of two-dimensional layered transition metal dichalcogenide nanosheets. *Nat. Chem.* **5**, 263–275 (2013).
44. J. Xia, F. Chen, J. Li, N. Tao, Measurement of the quantum capacitance of graphene. *Nat. Nanotechnol.* **4**, 505–509 (2009).